Research article

Lachlan M. Oberg, Eric Huang, Prithvi M. Reddy, Audrius Alkauskas, Andrew D. Greentree, Jared H. Cole, Neil B. Manson, Carlos A. Meriles and Marcus W. Doherty*

Spin coherent quantum transport of electrons between defects in diamond

https://doi.org/10.1515/nanoph-2019-0144
Received May 16, 2019; revised August 4, 2019; accepted August 5, 2019

Abstract: The nitrogen-vacancy (NV) color center in diamond has rapidly emerged as an important solid-state system for quantum information processing. Whereas individual spin registers have been used to implement small-scale diamond quantum computing, the realization of a large-scale device requires the development of an on-chip quantum bus for transporting information between distant qubits. Here, we propose a method for coherent quantum transport of an electron and its spin state between distant NV centers. Transport is achieved by the implementation of spatial stimulated adiabatic Raman passage through the optical control of the NV center charge states and the confined conduction states of a diamond nanostructure. Our models show that, for two NV centers in a diamond nanowire, high-fidelity transport can be achieved over distances of order hundreds of nanometers in timescales of order hundreds of nanoseconds. Spatial adiabatic passage is therefore a promising option for realizing an on-chip spin quantum bus.

Keywords: diamond; STIRAP; quantum transport.

***Corresponding author: Marcus W. Doherty,** Laser Physics Center, Research School of Physics and Engineering, Australian National University, Australian Capital Territory 2601, Australia, e-mail: marcus.doherty@anu.edu.au. https://orcid.org/0000-0002-5473-6481.
Lachlan M. Oberg, Eric Huang, Prithvi M. Reddy and Neil B. Manson: Laser Physics Center, Research School of Physics and Engineering, Australian National University, Australian Capital Territory 2601, Australia. https://orcid.org/0000-0002-4560-1833 (L.M. Oberg)
Audrius Alkauskas: Center for Physical Sciences and Technology, Vilnius LT-10257, Lithuania
Andrew D. Greentree: ARC Center of Excellence for Nanoscale BioPhotonics, School of Science, RMIT University, Melbourne, Victoria 3001, Australia
Jared H. Cole: Chemical and Quantum Physics, School of Science, RMIT University, Melbourne, Victoria 3001, Australia
Carlos A. Meriles: Department of Physics, CUNY-City College of New York, New York, NY 10031, USA

1 Introduction

Diamond-based quantum information processing (QIP) is possible due to the remarkable properties of the nitrogen-vacancy (NV) defect center. The spin states of individual NV centers can be optically addressed for initialization and read-out [1] and possess the longest room-temperature spin-coherence time of any solid-state defect [2]. Cryogenic temperatures further enhance these spin properties by up to four orders of magnitude [3] and enable spin-photon entanglement through coherent optical transitions [4]. This includes the adiabatic control of the NV spin using optical pulses [5]. These properties have been used to operate individual spin registers for small-scale quantum computing, including demonstrations of error correction [6], simple algorithms [7], and simulations [8]. Spin registers have been realized through clusters of NV centers as well as single NV centers coordinated with clusters of paramagnetic defects such as ^{13}C atoms and substitutional nitrogen (N_S) centers [9–15].

Individual spin registers are ultimately limited by the number of paramagnetic defects addressable by a single NV center (5–10 strongly coupled qubits [16]). The development of large-scale QIP therefore requires the use of quantum buses to entangle a network of interconnected clusters. At cryogenic temperatures, optical quantum buses have been used to entangle spin registers separated by macroscopic distances [4, 17, 18]. Unfortunately, this option is challenging for scalable QIP as optical buses are difficult to compactly incorporate on chip while maintaining low losses. One scalable suggestion is intracluster spin transport along a chain of paramagnetic defects [19, 20]. Despite the promise of room-temperature operation, engineering the spin chain is difficult with existing fabrication techniques. Recently, Doherty et al. [21] have proposed entanglement using semiclassical electron transport between two NV^{-}–$^{14}N_S$ pairs embedded in a diamond nanowire. This scheme is severely limited as semiclassical transport in a nanowire is prone to erroneous capture from N_s^+ defects, surface traps [22], or surface emission [23].

Consequently, here we propose an on-chip spin quantum bus for diamond QIP using spatial stimulated adiabatic Raman passage (STIRAP). Spatial STIRAP involves the transport of massive particles between spatially distinct locations using conventional STIRAP-type coupling. It was originally explored in the context of electronic transfer in double quantum dots [24, 25] and for general methods of spatial adiabatic passage, which promise robust quantum information transport [26, 27]. The conventional STIRAP technique is a method of population transfer between the two lowest levels of a Λ-type atomic system [28]. By applying optically coupling fields in the so-called counterintuitive direction, where the unpopulated transition is coupled before the populated transition, the system can be maintained in the optical dark state, which suppresses population in the central (excited) state. This suppression of population in the central state, which will ideally have zero population in the adiabatic limit, leads to the suppression of the effects of spontaneous emission. In the context of NV centers, STIRAP has been proposed [29] and demonstrated [30] for single qubit control; however, we are not aware of any proposals for the spatial transport of electrons between NV centers of the form considered here.

In our proposal for spatial STIRAP, the two disconnected states of the Λ scheme correspond to an electron occupying one of two distant NV centers embedded in a diamond nanostructure. As depicted in Figure 1A, we envision mediating adiabatic passage through states of the conduction band minimum, which are discretized by the confining potential of the nanostructure. While all nanostructures lead to discretization, we will consider nanowires as an archetypal structure. We have identified two different designs for realizing a nanowire confining potential, via the potential of a diamond surface or an electrostatic potential applied by electrodes in a bulk structure. The schematics for the transport scheme in these designs are presented in Figure 1. Although STIRAP is performed similarly in both cases, the susceptibility to different decoherence mechanisms varies. We also predict that quantum transport will maintain coherence of the electron's spin. Spin transport is known theoretically to be excellent in diamond due to an indirect band-gap, low spin-orbit coupling, low electron-phonon (e-p) scattering, and low background impurity spins [31]. Here, under STIRAP we explicitly exploit the low background impurities and low spin-orbit coupling of the conduction band to achieve spin coherent transport.

This proposal for quantum transport is fundamentally different from existing schemes for spatial STIRAP. As coupling is mediated optically rather than through the

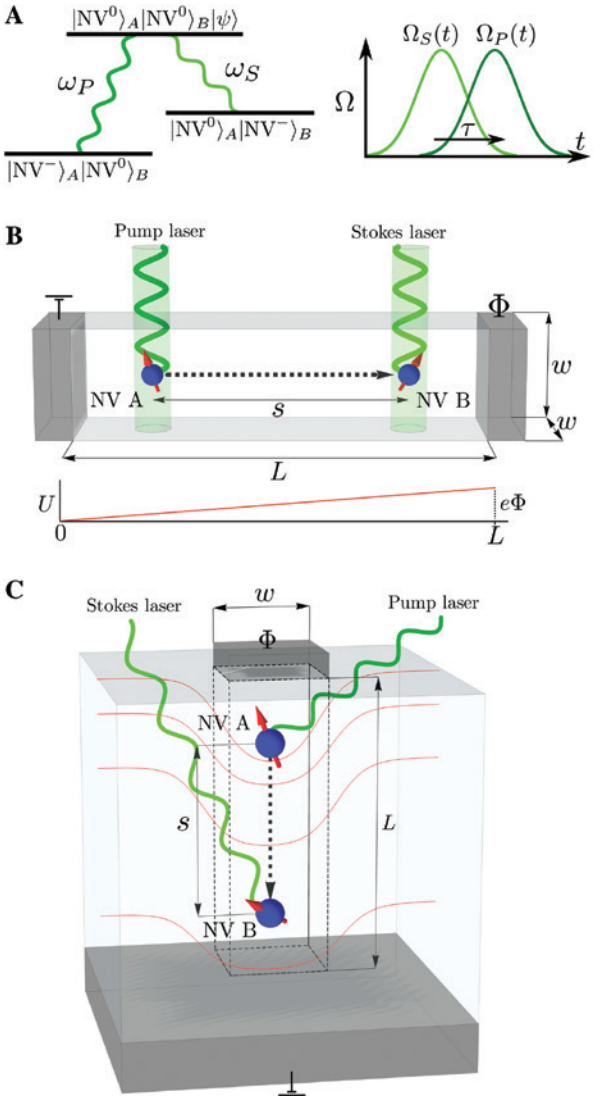

Figure 1: Design schematics for quantum transport of an electron between NV centers using STIRAP.
(A) Λ-level scheme for two NV centers in a diamond nanowire. Adiabatic passage is mediated by mutual coupling to the conduction band minimum state, $|\psi\rangle$. Applying a Stokes laser pulse before a pump laser pulse with some overlapping time τ results in adiabatic quantum transport of the electron and its spin state from NV *A* to NV *B*. (B) Two NV centers labeled *A* and *B* are separated by a distance *s* in a surface confined nanowire of length *L* and width *w*. A potential difference of Φ is applied to electrode plates affixed to either end of the wire. This generates a gradient electric potential (graphed as *U*), which lifts the degeneracy of states $|NV^-\rangle_A|NV^0\rangle_B$ and $|NV^0\rangle_A|NV^-\rangle_B$ in the STIRAP level scheme. To avoid erroneous excitations to higher conduction band states, the pump and Stokes lasers must individually address each NV center and therefore be spatially separated. (C) Schematic of an electrostatically confined nanowire. The two NV centers are aligned coaxial and perpendicular to the surface of a diamond substrate. A square nanoelectrode of width *w* is affixed to the surface above the NV centers, whereas a grounded electrode plate is affixed to the opposite side of the substrate. Applying a small positive voltage Φ to the nanoelectrode generates a nanowire confining potential (red equipotentials), which extends an effective depth *L* into the substrate.

manipulation of tunneling amplitudes [27], the spatially separated states are truly disconnected and there is no occupation of the intermediary space during transport. In this sense, it is colloquially akin to the teleportation of a massive particle. Furthermore, to our knowledge, this is the first spatial STIRAP proposal that includes coherent spin transport.

In Section 1, we present a proposal for implementing STIRAP in a diamond nanowire including a spin initialization and a measurement protocol. These spin protocols play the essential role of identifying the transported electrons (thereby distinguishing them from background sources) and will be the means for which spin entanglement is mediated. We identify a feasibility condition for transport, $\Delta E_c/\hbar \gg \Omega \gg \Gamma$, where ΔE_c defines the energy gap between the first and second conduction states, Ω is the Rabi frequency of the optical transition between defect and conduction states, and Γ is the optical decoherence rate. As a conservative estimate, these constraints can be considered satisfied when $\Delta E_c/\hbar \gtrsim 10\Omega \gtrsim 10\Gamma$. In Section 2, we calculate ΔE_c by modeling the effect of the nanowire confining potential on the diamond conduction band. Effective mass theory (EMT) is used to derive a level scheme and determine the energies of discretized conduction states. In Section 3, we present the first *ab initio* calculations for the photoionization mechanism of the NV center. This is used to evaluate values of Ω that can be practically achieved. We then identify optical decoherence mechanisms that contribute to Γ. Finally, in Section 4, we evaluate Ω, ΔE_c, and Γ at cryogenic temperatures for both nanowire designs introduced previously. The dimensions of the wires are optimized to maximize the Rabi frequency relative to decoherence and to satisfy the STIRAP feasibility constraints.

2 Quantum transport in diamond nanowires

STIRAP is a method for evolving a three-state system from an initial state $|1\rangle$ to a final state $|3\rangle$ [28, 32]. This is achieved through coupling to a mutual intermediary state, $|2\rangle$, although the direct transition $|1\rangle \rightarrow |3\rangle$ may be forbidden. To do so, a pump laser pulse with Rabi frequency $\Omega_P(t)$ is tuned to the $|1\rangle \rightarrow |2\rangle$ transition, whereas a Stokes laser pulse with Rabi frequency $\Omega_S(t)$ is tuned to the $|2\rangle \rightarrow |3\rangle$ transition. Applying the Stokes laser pulse before the pump laser pulse with some overlapping time τ results in an adiabatic evolution of the state from $|1\rangle \rightarrow |3\rangle$ without any population of $|2\rangle$. The requirement for adiabaticity is given by $\Omega\tau \gg 1$, where $\Omega^2 = \Omega_P^2 + \Omega_S^2$ is the effective Rabi frequency.

We propose using STIRAP for quantum transport of an electron between two NV centers. In Figure 1, NVs are embedded within the nanowire confining potential and labeled as *A* and *B*. This allows us to define a three-level system given by

$$|1\rangle = |\mathrm{NV}^-\rangle_A |\mathrm{NV}^0\rangle_B$$
$$|2\rangle = |\mathrm{NV}^0\rangle_A |\mathrm{NV}^0\rangle_B |\psi\rangle$$
$$|3\rangle = |\mathrm{NV}^0\rangle_A |\mathrm{NV}^-\rangle_B,$$

where $|\mathrm{NV}^-\rangle$ and $|\mathrm{NV}^0\rangle$ correspond to the $^3A_2$ and ^2E electronic ground states of the negative and neutral charge states of the NV centers and $|\psi\rangle$ is a nanowire conduction band minimum state. A schematic of the STIRAP level scheme is presented in Figure 2. The adiabatic passage between states $|1\rangle$ and $|3\rangle$ therefore constitutes the electron transport from NV *A* to NV *B* with no occupation of the intermediary space. The degeneracy of states $|1\rangle$ and $|3\rangle$ may be lifted by applying a potential difference Φ between each end of the length *L* wire. For a defect separation distance *s*, this induces an energy splitting of $\Delta E_d = e\Phi s/L$.

Let us now consider the transportation of the electron spin during STIRAP. This requires a protocol for spin initialization of both $|\mathrm{NV}^-\rangle_A$ and $|\mathrm{NV}^0\rangle_B$, which we now present in turn. First, suppose we wish to transport the spin-state $|\uparrow\rangle$. We restrict our attention to photoionization by

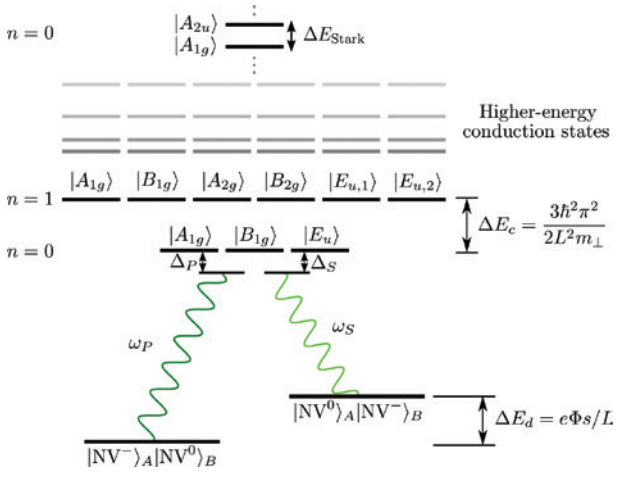

Figure 2: Nanowire energy-level diagram for the STIRAP transport protocol.
The electron is transported from the initial defect state $|\mathrm{NV}^-\rangle_A |\mathrm{NV}^0\rangle_B$ to the target defect state $|\mathrm{NV}^0\rangle_A |\mathrm{NV}^-\rangle_B$ using laser pulses with Rabi frequencies Ω_P and Ω_S to mediate adiabatic passage with the fourfold degenerate conduction band minima states. Implicit in the labeling of conduction band states is the combined electronic state of the defects, $|\mathrm{NV}^0\rangle_A |\mathrm{NV}^0\rangle_B$. Not to scale.

absorption of a single photon from an optical pulse and do not consider the two-photon ionization process of the NV^- [33]. As the ionizing pulse cannot differentiate between the two electrons occupying the *e*-orbitals of $|NV^-\rangle_A$, both must be initialized into $|\uparrow\rangle$. This can be achieved through the optical polarization of $|NV^-\rangle_A$ into the $m_s=0$ triplet state followed by the application of a microwave control pulse. The resulting spin-state can be expressed in the two *e*-orbital basis as $|+1\rangle=|\uparrow\rangle|\uparrow\rangle$. Hence, through this protocol, we can guarantee the ionization of a spin-up electron during STIRAP.

Now, consider the initialization of the $|NV^0\rangle_B$ spin-state. After STIRAP, electron transportation can only be validated if the read-out of the $|NV^-\rangle_B$ spin-state agrees with the spin initialized at $|NV^-\rangle_A$. Otherwise, it is impossible to discern if the charging of $|NV^0\rangle_B$ into $|NV^-\rangle_B$ was instead due to the erroneous electron capture. It is therefore essential for the read-out that $|NV^0\rangle_B$ is initialized into either the $|\uparrow\rangle$ or $|\downarrow\rangle$ spin eigenstates. To see how this could be achieved, consider that the $|NV^-\rangle_B$ spin-state after transport (assuming $|NV^0\rangle_B$ was initialized as $|\uparrow\rangle$) is given by $|\uparrow\rangle|\uparrow\rangle=|+1\rangle$. Similarly, we obtain the $m_s=0$ triplet-state when $|NV^0\rangle_B$ is initialized as $|\downarrow\rangle$. Transport can then be confirmed by performing read-out of the spin state at NV *B*.

The spin initialization of NV *B* can be achieved as follows. Consider NV *B* initially prepared into the negative charge state with spin projection $m_s=+1$. The application of a >2.6 eV photoionizing pulse will then eject an electron with $|\uparrow\rangle$ spin, leaving NV *B* in the neutral charge state with $|\uparrow\rangle$ spin. Equivalently, the $|\downarrow\rangle$ spin state can be prepared for NV *B* prepared in the $m_s=-1$ state. Although not proven, it is assumed that photoionization is a spin-conserving process. Even if this is not the case, one way to ameliorate the risk of nonconserving spin transitions is to polarize the N nuclear spin when NV *B* is in the negative charge state. After the ionizing pulse, this nuclear spin polarization can be swapped back onto the electron spin of the neutral charge state via microwave control. Such a scheme is now feasible given that recent progress has identified the NV^0 spin Hamiltonian [34].

Transportation also requires that NV^0 spin relaxation is long with respect to the STIRAP operation time. As of yet, the spin relaxation of the NV^0 ground state has not been directly observed due to the apparent absence of an electron paramagnetic resonance (EPR) signal [35]. Although this could potentially imply a high rate of spin relaxation, the new work by Barson et al. indicated that this is likely not the case. Rather, the apparent absence of an EPR signal is due to strain broadening in ensembles [34]. Drawing analogy between the similar electronic groundstates of the NV^0 and $Si\text{-}V^-$ centers, we expect spin relaxation to be not overly fast. This is because within the $Si\text{-}V^-$ center, e-p scattering is known to cause spin dephasing but not relaxation [36]. Consequently, at cryogenic temperatures, NV *B* should maintain its spin projection throughout transport.

During transport, spin decoherence mechanisms can be neglected. This remains true as long as the spin-quantization axis of the conduction states match those of the NV center and there is no rapid spin dephasing of these conduction states. This is investigated in Supplementary Section B, where we present symmetry arguments within the closure approximation. We prove that if the NV is coaxial to the wire, then the spin-quantization axis is conserved throughout STIRAP. Conveniently, NV centers can be preferentially aligned with a (111) wire axis during fabrication with chemical vapor deposition (CVD) [37]. For other nanowire directions, the spin-quantization axis of the conduction state can be aligned with the NV center via the application of a magnetic field. The magnitude of this field must be sufficiently large relative to the component of the spin-orbit interaction orthogonal to (111).

There are two further requirements for the successful implementation of STIRAP. First, coherent transport demands that there be no off-resonant coupling to states other than the conduction band minimum. Hence, the energy splitting between the first and second conduction states ΔE_c must be significantly greater than the Rabi frequency, $\Delta E_c/\hbar \gg \Omega$. Second, the optical decoherence rate Γ sets a bound on Ω, as it induces an unknown phase on the electron wave function as the transition energy fluctuates. Provided that the Rabi frequency is large ($\Omega \gg \Gamma$), this dephasing will be sufficiently small to achieve high-fidelity transport. The following two sections address each of these feasibility requirements in turn. We first investigate the effects of wire confinement on the conduction band before evaluating the Rabi frequency and identifying sources of optical decoherence.

3 Diamond nanowire conduction band

The confining potential of the nanowire leads to the discretization of the conduction band suitable for STIRAP. These confinement effects are well described through EMT [38], as detailed in Supplementary Section A. As shown in Figure 1, the nanowire was modeled as a square prism of monocrystalline diamond with dimensions of

$w \times w \times L$ ($w < L$). The two NV centers are separated by a distance s and located on the longitudinal. Consider that bulk diamond possesses six equivalent conduction band minima located at the k-points $\vec{K}_i$ between the Γ and X points in each orthogonal axis of the fcc Brillouin zone. The dispersion relationship at each $\vec{K}_i$ is modeled using diamond's anisotropic mass tensor and is referred to as a valley [39].

In the effective mass framework, the nth conduction band state for the ith valley of the nanowire is given by

$$\psi_{n,i}(\vec{r}) = F_{n,i}(\vec{r}) e^{i\vec{K}_i \cdot \vec{r}} u_i(\vec{r}), \tag{1}$$

where $F_{n,i}$ is an envelope function determined by the confining potential and u_i is the bulk-diamond Bloch function. For simplicity, we approximate the confining potential as an infinite square well. Although more realistic confining potentials such as a finite well would result in perturbations to the electronic structure, the key features are well described within our approximate model. This leads to the following envelope function

$$F_{n,i} = \sqrt{\frac{8V_c}{w^2 L}} \sin\left(\frac{n_x \pi x}{w}\right) \sin\left(\frac{n_y \pi y}{w}\right) \sin\left(\frac{n_z \pi z}{L}\right), \tag{2}$$

where $n = (n_x, n_y, n_z)$ and V_c is the volume of the diamond unit cell.

The true eigenstates of the nanowire conduction band are linear combinations of the valley wavefunctions (1), which respect to its D_{4h} symmetry. As presented in Supplementary Section A, symmetry analysis reveals four degenerate conduction band minima states formed from the valleys with $\vec{K}_i$ perpendicular to the wire axis (with symmetries A_{1g}, B_{1g}, and E_u). Similarly, the valley states with $\vec{K}_i$ parallel to the wire axis form degenerate eigenstates with A_{1g} and A_{2u} symmetry. For $L \gg w$, the energy of the twofold degenerate states exceeds that of the fourfold degenerate states, so only the latter are relevant for STIRAP. For the simple case of a wire aligned along a (100) axis, the eigenenergies of the fourfold conduction band minima states are given by

$$E_n = \frac{\hbar^2 \pi^2}{2} \left(\frac{n_x^2}{m_\parallel w^2} + \frac{n_y^2}{m_\perp w^2} + \frac{n_z^2}{m_\perp L^2} \right), \tag{3}$$

where $m_\perp$ and $m_\parallel$ are the transverse and longitudinal effective masses of an electron in bulk diamond. For $L \gg w$, this corresponds to

$$\Delta E_c = \frac{3\hbar^2 \pi^2}{2 m_\perp L^2}. \tag{4}$$

In Section 4, we use Equation (4) to assess the feasibility condition $\Delta E_c / \hbar \gg \Omega$ for the two different nanowire designs.

EMT is limited as it cannot account for coupling between valley states via the wire confining potential. Known as the valley-orbit interaction, this coupling leads to a fine splitting of the conduction band minima states [40]. Although the resulting eigenstates may be determined by symmetry, the magnitude of the splitting is notoriously difficult to quantify but assumed to be small [41–44]. A proper treatment would require detailed *ab initio* calculations, which are left as an opportunity for future work. The final electronic consideration is splitting induced by the applied electric field. As explored in Supplementary Section A, this Stark effect does not influence the states of the conduction band minimum. Although it does produce a small splitting of the A_{1g} and A_{2u} states, for $L \gg w$, this poses no impediment to the performance of STIRAP.

4 Optical processes in diamond nanowires

Assessing the feasibility of STIRAP requires comparing attainable photoionization Rabi frequencies to optical decoherence mechanisms. In this section we first present calculations of the photoionization Rabi frequency including Franck-Condon effects. We then identify and characterize three optical decoherence mechanisms; erroneous capture by N_s^+ defects, e-p scattering and spontaneous emission.

4.1 Photoionization Rabi frequency

The conduction dipole moment was first obtained for the photoionization of bulk NV centers using *ab initio* calculations. Density functional theory was performed using the VASP plane-wave code with a 512-atom diamond supercell [45–48] and Heyd-Scuseria-Ernzerhof functionals [49]. The energy of the $^3A_2$ ground state of the NV^- center and the ^2E ground state of the NV^0 center (plus an ionized electron) were calculated as a function of generalized atomic coordinates. As detailed in Supplementary Section C, the calculations produced an ionization energy of $\omega = 2.6$ eV (close to experimental values [33]) and a Huang-Rhys factor of $S = 1.39$. The direct calculation of the optical matrix elements yields a transition dipole moment of $d_{\text{bulk}} = 0.085e$ Å, normalized to the volume of the 512-atom supercell.

The bulk photoionization dipole moment can be used to determine the corresponding moment in a nanowire. Noting that this moment is identical for both the pump and Stokes pulse, we calculate in Supplementary Section C that

$$d_{\text{wire}} = F_0(\vec{R}_A)e^{-S/2}d_{\text{bulk}}, \tag{5}$$

where $\vec{R}_A$ is the position of NV A. For defects centered at opposite ends of the wire, the normalization function in Equation (5) can be simplified as

$$F_0(s) = \sqrt{\frac{8V_{\text{sc}}}{w^2 L}}\cos\left(\frac{\pi s}{2L}\right), \tag{6}$$

where $V_{\text{sc}} = 2.837$ nm^3 is the volume of the 512-atom supercell. Assuming a laser power P with radial spot-size r, the effective photoionization Rabi frequency within a diamond nanowire is

$$\Omega = \frac{e^{-S/2}}{r\hbar}\sqrt{\frac{8P}{n_D c\varepsilon_0 \pi}}F_0(s)d_{\text{bulk}}, \tag{7}$$

where n_D is the index of refraction in diamond. The achievable spot size and power are related to each other depending on the technical aspects of the optics employed. A conservative estimate says that a diffraction-limited spot size $r = 200$ nm can be attained with a lasing power of $P = 100$ mW. These parameters will be used in Section 4 to evaluate the photoionization Rabi frequency.

4.2 Decoherence mechanisms

One source of optical decoherence is the erroneous capture of conduction band electrons by N_s^+ defects. Typically, N_S defects are formed during CVD growth due to N-based gases present in the plasma [50]. These defects act as electron donors, readily ionizing to N_s^+ to fill electron traps from surface defects [22]. The N_s^+ capture rate can be estimated as $\Gamma_{\text{cap}} = \rho_{N_S^+}\rho_e L^2 w\sigma\sqrt{k_B T/m^*}$, where $\sigma \approx 3$–7 nm^2 is the N_s^+ capture cross-section, k_B is the Boltzmann constant, T is the temperature, $m^\star$ is the isotropic mean of the effective mass components, $\rho_{N_S^+}$ is the density of N_s^+ defects, and ρ_e is the probability density of the conduction band states [21].

We may conservatively estimate that $\rho_e L^2 w < 1$; thus, the capture rate is independent of volume. Assuming that $T = 4$ K and $\rho_{N_S^+} \approx 1$ ppb, we find that $\Gamma_{\text{cap}} \lesssim 2.5$ MHz. This places a constraint on the photoionization Rabi frequency for STIRAP in any nanostructure. In this analysis, we have assumed passivation of all surface traps by N_S donors. If this is not the case, surface defects must be considered as another source of electron capture. Other defects, such as vacancy clusters introduced during fabrication, may also act as electron traps. However, they will not be dominant in number within a single wire in comparison to N_S defects.

A second source of decoherence can be attributed to the e-p scattering of the conduction band states. We consider only first-order processes involving absorption and emission of acoustic phonons with higher-energy conduction states. Higher-order interactions can be considered negligible at 4 K. The e-p scattering rate, Γ_{ep}, may be determined through Fermi's golden rule with the Hamiltonian

$$\hat{\mathcal{H}}_{\text{ep}} = \Xi_d \vec{\nabla}\cdot\vec{u}_f, \tag{8}$$

where $\Xi_d = 8.7$ eV is the diamond deformation potential [51] and $\vec{u}_f$ is the nanowire phonon field. Explicit rates for Γ_{ep} are specific to the nanowire design and are presented in the following section.

A fundamental source of optical decoherence is that due to spontaneous emission. The spontaneous emission rate for transitions $|2\rangle \rightarrow |1\rangle$ and $|2\rangle \rightarrow |3\rangle$ may be estimated using conventional expressions as [52]

$$\Gamma_{\text{SE}} = 2\frac{\omega^3 d_{\text{wire}}^2}{3\pi\varepsilon_0 n\hbar c^3}. \tag{9}$$

note that this decoherence rate is dependent on wire geometry through the normalization function F as per Equation (5). We now evaluate the Rabi frequency and total decoherence rate within both nanowire designs – surface confinement and electrostatic confinement – and optimize wire dimensions to satisfy the STIRAP feasibility conditions.

5 Optimization of nanowire design

5.1 Surface confinement

As displayed in Figure 1A, electronic confinement may be realized through the fabrication of freestanding nanowires [53, 54] or nanopillars [55] using reactive ion etching. To avoid injection of spurious electrons, it is necessary that the electrodes affixed to the wire ends are insulating and separated from the diamond surface with a high resistivity contact. NV centers may be introduced into wires through either N ion-implantation [56, 57] or N δ-doping [58].

A pair of NV centers suitable for STIRAP can then be identified by confocal microscopy. Ideally, the NVs will be coaligned along a (111) axis and situated at depths greater than ~50 nm (this is necessary for obtaining optimal bulk-like properties [59]).

We now derive an expression for the decoherence rate due to e-p scattering. In Supplementary Section D, we present calculations of Γ_{ep} by approximating $\vec{u}_f$ through the elasticity theory. Acoustic nanowire phonon modes may be classified as dilational, flexural, torsional, and shear [60]. However, only dilational modes possess nonzero divergence and contribute to the e-p scattering as per Hamiltonian (8). The dilational modes $\vec{u}_{d,m}$ have angular frequencies quantized by $m=(m_x, m_y, m_z)$, which are given by

$$\omega_m^2 = \pi^2 c_l^2 \left(\frac{m_x^2 + m_y^2}{w^2} + \frac{m_z^2}{L^2} \right), \tag{10}$$

where c_l is the longitudinal speed of sound in diamond. The scattering rate can then be calculated as

$$\Gamma_{ep} = \frac{2\pi}{\hbar^2} \sum_{n,m} \Xi_d^2 |M_{n,m}|^2 \frac{\hbar}{2\rho_C w^2 L \omega_m} \times n_B(\omega_m, T) \rho(\omega_n - \omega_m), \tag{11}$$

where $M_{n,m}$ is the overlap integral between the electron and phonon wavefunctions, ρ_C is the density of diamond, and n_B is the Bose-Einstein distribution. The density of states, ρ, is assumed to be a Lorentzian, given by

$$\rho(\omega_n - \omega_m) = \frac{\gamma/\pi}{(\omega_n - \omega_m)^2 + \gamma^2}, \tag{12}$$

where $\gamma \approx \omega_m/Q$ for Q is the quality factor. For diamond microcantilevers, $Q > 10^6$ has been observed [61].

We now optimize the dimensions of a surface-confined nanowire with respect to the STIRAP feasibility condition $\Delta E_c/\hbar \gg \Omega \gg \Gamma$. In Figure 3A, we present the photoionization Rabi frequency derived in Equation (7) as a function of wire dimension. In Figure 3B, we compare the Rabi frequencies to the total decoherence rate $\Gamma = \Gamma_{cap} + \Gamma_{SE} + \Gamma_{ep}$ for varying nanowire dimensions. We assume that $Q = 10^6$, $T = 4$ K and that each NV center is positioned 100 nm from its respective wire end. For simplicity, we have only considered wires aligned along a (100) axis, although similar results likely hold for other wire directions.

Figure 3B indicates that, in general, decoherence effects are minimized for smaller wire dimensions. This can be attributed to the normalization of the Rabi frequency, which scales inversely proportional with wire volume as evident in Figure 3A [cf. Equation (7)]. The

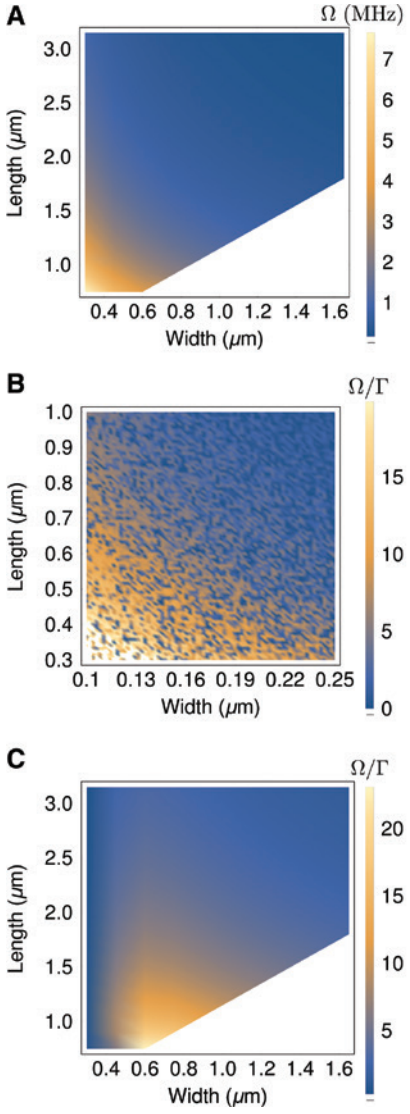

Figure 3: Dimensional dependence of optical properties within (100) aligned diamond nanowires.
(A) Density plot of the photoionization frequency Ω as a function of wire dimension. (B) Density plot of the ratio of the photoionization frequency to the optical decoherence rate (Ω/Γ) as a function of dimension for a surface confined nanowire. (C) Density plot of the ratio of the photoionization frequency to the optical decoherence rate (Ω/Γ) as a function of nanowire dimension for an electrostatically confined nanowire. Note that we have omitted calculations of Ω and Ω/Γ for wires with $w > L$.

sporadic variations in Ω/Γ can be attributed to the resonance between electronic and photonic levels. Consulting Equation (11), certain wire dimensions produce an increased density of resonant states, which amplifies the rate of e-p scattering. Off resonance, the dominant decoherence mechanism is electron capture. A range of wire dimensions with $L < 0.6$ μm and $w < 0.2$ μm satisfy the STIRAP feasibility condition with at least $\Omega > 10\Gamma$,

reaching a maximum of $\Omega \approx 20\Gamma$ for short wires 0.3 μm long. Note that for all wire dimensions considered in Figure 3B, $\Delta E_c/\hbar > 10^3\Omega$; therefore, off-resonant coupling does not pose an impediment to STIRAP.

5.2 Electrostatic confinement

An alternative means for realizing a nanowire confining potential is through electrodes in a bulk structure. Consider the diamond substrate presented in Figure 1B, where two coaligned NV centers can be identified through confocal microscopy. To generate the confining potential, a square nanoelectrode with width w is affixed to the surface directly above the NV centers. On the opposing surface of the diamond substrate, an electrode plate is fixed and grounded. Applying a positive potential to the square electrode will then generate a confining potential. This localizes the electron density near the surface into a wire-like geometry. The effective length of this wire may be tuned through the magnitude of the potential. Conveniently, the potential also generates an electric field gradient that can be used to energetically distinguish each NV center during STIRAP. These electrostatic properties are demonstrated through simulations using COMSOL Multiphysics software presented in Supplementary Section E.

In contrast to surface-confined wires, electron scattering within electrostatically confined wires is due to interactions with bulk phonons. The calculation of Γ_{ep} using Fermi's golden rule and the Hamiltonian (8) is presented in Supplementary Section D. We find that

$$\Gamma_{ep} = \frac{1}{2(2\pi)^2}\frac{\Xi_d^2}{\hbar\rho_C c_l^7}\sum_n \omega_n^5 n_B(\omega_n, T) \times \int_0^{\pi}\int_0^{2\pi} G_n\left(\frac{\omega_n}{c_l}, \theta, \phi\right)\sin(\theta)\mathrm{d}\theta\mathrm{d}\phi, \tag{13}$$

where G_n is a complicated expression for the overlap integral.

A further benefit of the electrostatic confinement design is that decoherence due to N_s^+ capture can be mitigated through the inclusion of a sacrificial donor layer. N_S defects distant from the confining potential can be δ-doped into the substrate during CVD growth [58]. The sacrificial defects donate electrons to the surface traps until charge conservation occurs, reducing the density of N_s^+ available for erroneous capture within the confining potential [22]. We conservatively estimate that the presence of a sacrificial layer can reduce Γ_{cap} by 95%.

In Figure 3C, we present the dimensional dependence of Ω/Γ for an electrostatically confined nanowire aligned along the (100) axis. We have that $G_n \propto w^{-4}$ in Equation (13); therefore, e-p scattering dominates the Rabi frequency for wire widths less than approximately 0.4 μm. For larger wire dimensions, both e-p scattering and spontaneous emission are negligible and the dominant source of decoherence is due to N_s^+ capture. The STIRAP feasibility conditions are satisfied when $0.5\ \mu\mathrm{m} < w < 0.9\ \mu\mathrm{m}$ and $0.75\ \mu\mathrm{m} < L < 1.25\ \mu\mathrm{m}$, which yields $\Omega > 10\Gamma$. The ratio Ω/Γ is optimized at ≈25 for wire dimensions of $L = 0.75$ μm and $w = 0.6$ μm. Furthermore, for all wire dimensions, $\Delta E_c/\hbar \gg 10^3\Omega$; hence, crosstalk with higher-energy states in the conduction band is negligible.

6 Conclusion

In this paper, we propose spatial STIRAP to realize an on-chip spin quantum bus for scalable diamond QIP devices. Our scheme considers coherent quantum transport of an electron and its spin state between two NV centers embedded in a diamond nanowire. This is achieved by implementing STIRAP for the optical control of the NV center charge states and the confined nanowire conduction states. In contrast to existing spatial STIRAP protocols that manipulate tunneling amplitudes between distant sites, our proposal realizes quantum transport without any occupation of the intermediary space. Furthermore, to our knowledge, this is the first implementation of spatial STIRAP including spin-state transport.

A proposal for our scheme was first presented along with a protocol for initializing the NV spin-states. We identified a feasibility condition for implementing STIRAP, $\Delta E_c/\hbar \gg \Omega \gg \Gamma$, requiring the photoionization Rabi frequency to exceed optical decoherence rates and be limited by coupling with higher-energy conduction states. For the latter, EMT was employed to model the effects of the nanowire confining potential on the diamond conduction band. We then presented the first *ab initio* calculations of the NV photoionization Rabi frequency. This allowed the STIRAP feasibility condition to be evaluated in two nanowire designs, which achieved electronic confinement through either a surface structure or electrodes. By optimizing the Rabi frequency relative to the decoherence rate for varying wire dimension, we conclude that STIRAP is feasible in both designs in timescales on the order of hundreds of nanoseconds.

The first experimental stages should perform photoionization spectroscopy to assess the spectral linewidth of discretized states in the nanowire conduction band. Ultimately, this will determine whether deterministic photoionization to the conduction band minimum is feasible.

A second key experiment is to directly the measure the spin-relaxation time of the NV^0 center to confirm that it is sufficiently long to enact the STIRAP protocol. This study has also introduced multiple avenues for future theoretical research. For example, a detailed *ab initio* model of the nanowire electronic structure would allow for the precise calculation of valley-orbit and spin-orbit interactions. This would require the development of new computational tools for simulating mesoscopic diamond structures.

Acknowledgments: We acknowledge funding from the Australian Research Council (DE170100169, DP170103098, FT160100357, and CE170100026). C.A.M. acknowledges the support from the National Science Foundation through grants NSF-1547830, NSF-1619896, and NSF-1914945 and the Research Corporation for Science Advancement through a FRED Award. A.A. acknowledges the funding from the European Union's Horizon 2020 Research and Innovation Programme under grant agreement no. 820394 (project Asteriqs). This research was undertaken with the assistance of resources and services from the National Computational Infrastructure, which is supported by the Australian Government.

References

[1] Doherty MW, Manson NB, Delaney P, et al. The nitrogen-vacancy colour centre in diamond. Phys Rep 2013;528:1–45.
[2] Balasubramanian G, Neumann P, Twitchen D, et al. Ultralong spin coherence time in isotopically engineered diamond. Nat Mater 2009;8:383–7.
[3] Jarmola A, Acosta VM, Jensen K, et al. Temperature- and magnetic-field-dependent longitudinal spin relaxation in nitrogen-vacancy ensembles in diamond. Phys Rev Lett 2012;108:197601.
[4] Togan E, Chu Y, Trifonov AS, et al. Quantum entanglement between an optical photon and a solid-state spin qubit. Nature 2010;466:730–4.
[5] Yale CG, Buckley BB, Christle DJ, et al. All-optical control of a solid-state spin using coherent dark states. Proc Natl Acad Sci 2013;110:7595–600.
[6] Taminiau TH, Cramer J, van der Sar T, et al. Universal control and error correction in multi-qubit spin registers in diamond. Nat Nanotechnol 2014;9:171–6.
[7] Shi F, Rong X, Xu N, et al. Room-temperature implementation of the Deutsch-Jozsa algorithm with a single electronic spin in diamond. Phys Rev Lett 2010;105.
[8] Wang Y, Dolde F, Biamonte J, et al. Quantum simulation of helium hydride cation in a solid-state spin register. ACS Nano 2015;9:7769–74.
[9] Gaebel T, Domhan M, Popa I, et al. Room-temperature coherent coupling of single spins in diamond. Nat Phys 2006;2:408–13.
[10] Hanson R, Mendoza FM, Epstein RJ, et al. Polarization and readout of coupled single spins in diamond. Phys Rev Lett 2006;97:087601.
[11] Neumann P, Mizuochi N, Rempp F, et al. Multipartite entanglement among single spins in diamond. Science 2008;320:1326–9.
[12] Neumann P, Kolesov R, Naydenov B, et al. Quantum register based on coupled electron spins in a room-temperature solid. Nat Phys 2010;6:249–53.
[13] Dolde F, Jakobi I, Naydenov B, et al. Room-temperature entanglement between single defect spins in diamond. Nat Phys 2013;9:139–43.
[14] Dolde F, Bergholm V, Wang Y, et al. High-fidelity spin entanglement using optimal control. Nat Commun 2014;5:3371.
[15] Waldherr G, Wang Y, Zaiser S, et al. Quantum error correction in a solid-state hybrid spin register. Nature 2014;506:204–7.
[16] Doherty M. The state of diamond quantum computing. Aust Phys 2017;110:7595–600.
[17] Bernien H, Hensen B, Pfaff W, et al. Heralded entanglement between solid-state qubits separated by three metres. Nature 2013;497:86–90.
[18] Hensen B, Bernien H, Dreaú AE, et al. Loophole-free Bell inequality violation using electron spins separated by 1.3 kilometres. Nature 2015;526:682–6.
[19] Yao NY, Jiang L, Gorshkov AV, et al. Scalable architecture for a room temperature solid-state quantum information processor. Nat Commun 2012;3:800.
[20] Nikolopoulos GM, Jex I. Quantum state transfer and network engineering. 2014:1–250.
[21] Doherty MW, Meriles CA, Alkauskas A, et al. Towards a room-temperature spin quantum bus in diamond via electron photoionization, transport, and capture. Phys Rev X 2016;6:041035.
[22] Stacey A, Dontschuk N, Chou JP, et al. Evidence for primal sp2 defects at the diamond surface: candidates for electron trapping and noise sources. Adv Mater Interfaces 2019;6:201801449.
[23] Kaviani M, Deák P, Aradi B, et al. Proper surface termination for luminescent near-surface NV centers in diamond. Nano Lett 2014;14:4772–7.
[24] Brandes T, Vorrath T. Adiabatic transfer of electrons in coupled quantum dots. Phys Rev B Condensed Matter Mater Phys 2002;66:753411–12.
[25] Vitanov NV, Rangelov AA, Shore BW, et al. Stimulated Raman adiabatic passage in physics, chemistry, and beyond. Rev Mod Phys 2017;89:015006.
[26] Greentree AD, Cole JH, Hamilton AR, et al. Coherent electronic transfer in quantum dot systems using adiabatic passage. Phys Rev B Condensed Matter Mater Phys 2004;70:1–6.
[27] Menchon-Enrich R, Benseny A, Ahufinger V, et al. Spatial adiabatic passage: a review of recent progress. Rep Prog Phys 2016;79:074401.
[28] Bergmann K, Theuer H, Shore BW. Coherent population transfer among quantum states of atoms and molecules. Rev Mod Phys 2002;70:1003–25.
[29] Coto R, Jacques V, Hétet G, et al. Stimulated Raman adiabatic control of a nuclear spin in diamond. Phys Rev B 2017;96:1003–25.
[30] Zhou BB, Baksic A, Ribeiro H, et al. Accelerated quantum control using superadiabatic dynamics in a solid-state lambda system. Nat Phys 2017;13:330–4.

[31] Restrepo OD, Windl W. Full first-principles theory of spin relaxation in group-IV materials. Phys Rev Lett 2012;109:166604.
[32] Ivanov PA, Vitanov NV, Bergmann K. Effect of dephasing on stimulated Raman adiabatic passage. Phys Rev A Atomic Mol Opt Phys 2004;70:063409.
[33] Aslam N, Waldherr G, Neumann P, et al. Photo-induced ionization dynamics of the nitrogen vacancy defect in diamond investigated by single-shot charge state detection. N J Phys 2013;15:013064.
[34] Barson MSJ, Krausz E, Manson NB, Doherty MW. The fine structure of the neutral nitrogen-vacancy center in diamond. Nanophotonics 2019;8:1985–91.
[35] Felton S, Edmonds AM, Newton ME, et al. Electron paramagnetic resonance studies of the neutral nitrogen vacancy in diamond. Phys Rev B Condensed Matter Mater Phys 2008;77:081201.
[36] Jahnke KD, Sipahigil A, Binder JM, et al. Electron-phonon processes of the silicon-vacancy centre in diamond. N J Phys 2015;17:043011.
[37] Michl J, Teraji T, Zaiser S, et al. Perfect alignment and preferential orientation of nitrogen-vacancy centers during chemical vapor deposition diamond growth on (111) surfaces. Appl Phys Lett 2014;104:102407.
[38] Stoneham AM. Theory of defects in solids. Acta Crystallogr Section A 1976;32:527.
[39] Madelung O. Semiconductors: data handbook. Microelectron J 2004;35:685.
[40] Murphy-Armando F, Fagas G, Greer JC. Deformation potentials and electron-phonon coupling in silicon nanowires. Nano Lett 2010;10:869–73.
[41] Resca L, Resta R. Large binding due to dispersive screening and Bloch function interference in many-valley semiconductors. Solid State Commun 1979;29:275–7.
[42] Resta R. A note on the many-valley effective mass theory. J Phys C Solid State Phys 1977;10.
[43] Luttinger JM, Kohn W. Motion of electrons and holes in perturbed periodic fields. Phys Rev 1955;97:869–83.
[44] Altarelli M, Hsu WY, Sabatini RA. Donor binding energies in multivalley semiconductors. J Phys C Solid State Phys 1977;10.
[45] Kresse G, Furthmüller J. Efficiency of ab-initio total energy calculations for metals and semiconductors using a plane-wave basis set. Comput Mater Sci 1996;6:15–50.
[46] Kresse G, Hafner J. *Ab initio* molecular-dynamics simulation of the liquid-metalamorphous-semiconductor transition in germanium. Phys Rev B 1994;49:14251–69.
[47] Kresse G, Furthmüller J. Efficient iterative schemes for *ab initio* total-energy calculations using a plane-wave basis set. Phys Rev B Condensed Matter Mater Phys 1996;54:11169–86.
[48] Kresse G, Joubert D. From ultrasoft pseudopotentials to the projector augmented-wave method. Phys Rev B Condensed Matter Mater Phys 1999;59:1758–75.
[49] Heyd J, Scuseria GE, Ernzerhof M. Hybrid functionals based on a screened Coulomb potential. J Chem Phys 2003;118:8207–15.
[50] Samlenski R, Haug C, Brenn R, et al. Incorporation of nitrogen in chemical vapor deposition diamond. Appl Phys Lett 1995;67:2798.
[51] Nava F, Canali C, Jacoboni C, et al. Electron effective masses and lattice scattering in natural diamond. Solid State Commun 1980;33:475–7.
[52] Fox M. Quantum optics: an introduction. 1st ed. Oxford: Oxford University Press, 2006.
[53] Babinec TM, Hausmann BJ, Khan M, et al. A diamond nanowire single-photon source. Nat Nanotechnol 2010;5:195–9.
[54] Burek MJ, de Leon NP, Shields BJ, et al. Free-standing mechanical and photonic nanostructures in single-crystal diamond. Nano Lett 2012;12:6084–9.
[55] Momenzadeh SA, Stöhr RJ, de Oliveira FF, et al. Nanoengineered diamond waveguide as a robust bright platform for nanomagnetometry using shallow nitrogen vacancy centers. Nano Lett 2015;15:165–9.
[56] Bayn I, Chen EH, Trusheim ME, et al. Generation of ensembles of individually resolvable nitrogen vacancies using nanometer-scale apertures in ultrahigh-aspect ratio planar implantation masks. Nano Lett 2015;15:1751–8.
[57] Pezzagna S, Wildanger D, Mazarov P, et al. Nanoscale engineering and optical addressing of single spins in diamond. Small 2010;6:2117–21.
[58] Ohashi K, Rosskopf T, Watanabe H, et al. Negatively charged NVC in a 5nm thin ^{12}C diamond film. Nano Lett 2013;13:4733–8.
[59] Ohno K, Joseph Heremans F, Bassett LC, et al. Engineering shallow spins in diamond with nitrogen delta-doping. Appl Phys Lett 2012;101.
[60] Nishiguchi N, Ando Y, Wybourne MN. Acoustic phonon modes of rectangular quantum wires. J Phys Condensed Matter 1997;9:5751–64.
[61] Tao Y, Boss JM, Moores BA, et al. Single-crystal diamond nanomechanical resonators with quality factors exceeding one million. Nat Commun 2014;5:3638.

Supplementary Material: The online version of this article offers supplementary material (https://doi.org/10.1515/nanoph-2019-0144).